2023 IEEE/ASME International Conference on
Advanced Intelligent Mechatronics (AIM)

Balance Gait Controller for a Bipedal Robotic Walker with Foot Slip

Marko Mihalec and Jingang Yi

***Abstract*—Low-friction ground conditions present a navigation challenge for bipedal robotic locomotion. While robots might traverse slippery surfaces by carefully planning trajectories, balance recovery from unexpected slip remains a challenge. We present a motion and gait control design for bipedal robotic walkers under foot slip. Slipping dynamics are explicitly considered as a part of the walker's dynamic model. A two-mass inverted pendulum model is presented to capture the ankle actuation effect and used to determine the gait recovery stepping location. A whole-body balance controller is then applied to realize the stepping task. The integration of the abstracted inverted pendulum model and the multi-link model helps build a whole-body operational space design to compute the controlled joint torques. We design a 5-link planar walking robot and implement the control system on the platform. A comprehensive set of walking experiments are presented, demonstrating the performance of the controller for walking on both high-, low- and extremely low-friction ground surfaces. The experimental results confirm that explicit consideration of foot slip improves the performance and yields a stable gait on a low-friction ground surface.**

***Index Terms*—Bipedal dynamics, robot control, slip dynamics, gait recovery, balance control**

I. Introduction

Bipedal robotic walkers bring immense potential for autonomy in unstructured environments [1]. When generating a walking gait, one of the most important factors to consider is the contact friction characteristic between the walker's foot and the ground. Most bipedal research work either assume non-slip contact or design gait and locomotion control to avoid foot slip [2]. Instead of a priori avoiding slip, this work acknowledges that foot slip might occur for bipedal robots that interact with environments and that robots are in danger of loosing balance and falling. We explicitly consider the possible presence of foot slip and present a gait controller under which the robot performs stable walking gaits under foot slip disturbances.

Due to the high-dimensional bipedal robots and the complexity of the walking task, a gait controller is usually constructed hierarchically [3]. For high-level motion or trajectory planning, the robot controllers are built on reduced-order or abstracted models, whereas a low-level control system uses high-fidelity full-body dynamics to compute joint torques to allow the biped to follow a planned motion. One commonly used simplified model for bipedal robotic walkers is the linear inverted pendulum (LIP) [4]–[6]. Due to its simplicity, the LIP model lends itself to compact, closed-form solutions, which are conveniently used for motion analysis and real-time motion planning. Using concepts such as capture point (CP) [7], it has been demonstrated model's capability for synthesizing stable gaits [8]–[11]. The LIP model usually assumes that all the mass is concentrated at a single point of the center of mass (COM) and the vector of ground reaction forces has to always point through the COM. As a result, the angular inertia around the COM is negligible and this property prevents using the ankle actuation as part of control correction under foot slip. Consequently, several revised LIP models were proposed to circumvent the above-mentioned restriction for studying foot slip dynamics [12]. In this work, we use the two-mass linear inverted pendulum (TMLIP) model that was introduced in [13] to design the foot placement design under slip. The TMLIP model was demonstrated as an effective tool for human normal walking and slipping gaits [14].

While the high-level LIP model provides a tool to plan the COM trajectory or foot placement, a low-level full-body controller is needed to realize the simplified tasks for joint torque control. In this work, we use a variation of the whole-body operational space (WBOS) framework [15]. In the WBOS, the target behavior is specified in the task space and that allows for specification of multiple kinematics tasks. By doing so, the inverse dynamics problem is fully determined and solved efficiently. The support consistent null space is used to map the set of tasks from the task space to the joint space and to obtain the desired joint torques using the inverse system dynamics. This approach was recently demonstrated to yield stable dynamic walking in a simulation of a bipedal robot control [16]. Similarly, the work in [17] proposed a hierarchical control structure that used the operational space framework and proved robust in the presence of external disturbances. We extend the method by introducing a frictional WBOS (FWBOS), where the conventional no-slip assumption is relaxed and a Coulomb friction model is used to model the slipping motion between the foot and the ground. A variation of the FWBOS-based controller was presented in [18] and demonstrated increased robustness for walking on slippery surfaces in simulation only.

Most of research work that study slip dynamics focus on human gait and walking (e.g., [12], [14], [19]). It is still unclear how to design gait recovery control for bipedal robotic walkers. The stability of a compass biped gait under slip conditions was studied in [20] without experimental validation. The work in [21] presented an integrated inverted pendulum

The work was supported in part by the US NSF under award CMMI-1762556.

M. Mihalec was with the Department of Mechanical and Aerospace Engineering, Rutgers University, Piscataway, NJ 08854 USA and is now with ASML, Wilton, CT 06897 USA (email: marko.mihalec@rutgers.edu).

J. Yi is with the Department of Mechanical and Aerospace Engineering, Rutgers University, Piscataway, NJ 08854 USA (email: jgyi@rutgers.edu).

model with the FWBOS control but no experimental validation. Recent work demonstrated adaptations of robot gait to prevent slip on low-friction surfaces [22]. Robotic walking with explicit consideration of foot slip was presented in [23]; however, the slip was expected and planned in advance. In this paper, we demonstrate stable bipedal robot walking in presence of unexpected slip on low-frictional surfaces. The TMLIP model is integrated with the FWBOS framework to provide the high-level recovery step planning with the low-level joint torque control to implement the planned gait. We also demonstrate a mechatronic design of a robotic walker to validate the gait control under various slipping conditions.

The main contribution of this work is the integrated the two-mass LIP model-based motion planning and the full-body balance recovery control for bipedal robot under unexpected foot slip perturbation. We introduce the generalized CP for step planning in both slip and non-slip conditions. The CP-based planning allows safety-guaranteed balance gaits under unexpected foot slip. Moreover, the CP step planning with an FWBOS-based whole-body controller provides a new hierarchical control design for bipedal robots under foot slip perturbation. Moreover, the experimental demonstration of the bipedal robot control under foot slip is new. To our best knowledge, no other model-based slip control design has been reported for bipedal robots. Compared with the work presented in [18], this paper presents an integrated high- and low-level model-based hierarchical control design for bipedal robots, whereas with the work in [21], we demonstrate the mechatronic systems design and extensive experimental implementation.

The remainder of this paper is organized as follows. Section II presents the TMLIP model and the CP concept. Section III discusses the FWBOS-based gait recovery control design. We present the experimental setup in Section IV. Experimental results are included in Section V followed by the concluding remarks in Section VI.

II. TMLIP-Based Recovery Step Planning

Fig. 1 shows the schematic of the bipedal robot models. We consider an underactuated biped walker as shown in the figure. The robot shown is a 5-link bipedal walker that has five degrees of freedom (DOFs) and only four joints are actuated (i.e., two hip and two knee joints). Point contact is considered between the foot and the firm ground. Bipedal walking gait is dynamically stabilized by a set of properly positioned foot steps. When the foot touches down on the ground, the foot contact can slip and we need to design a gait recovery control.

A. Two-Mass LIP Model

A reduced-order linear inverted pendulum model is used to determine the location of subsequent step after one foot slips. We use the TMLIP model to design step planning. The left-side schematic in Fig. 1 illustrates the TMLIP model. The model consists of two point masses. Mass m_1 located at x_c represents the body weight and is equivalent to the widely used LIP model [4]. Point mass m_2 represents the lower part of the stance leg and is located at the contact point between the foot and the ground. Its horizontal location is denoted as x_s in the inertial frame. Similar to many other LIP models, we assume that the height of m_1, denoted by z_c, is constant and the bipedal robot's motion is only in the sigittal plane.

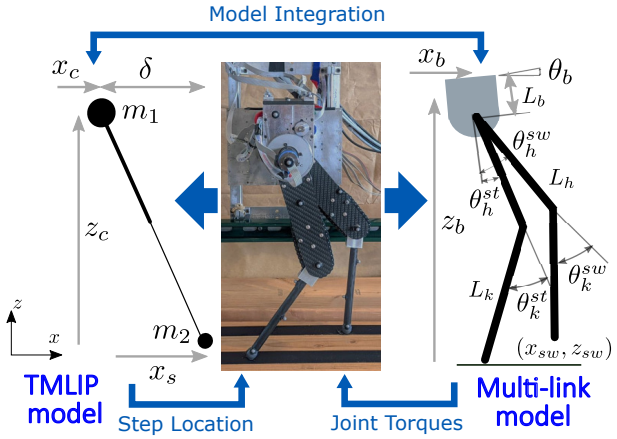

Fig. 1. Left: schematic of the TMLIP model. Center: bipedal robotic walker. Right: schematic of a 5-link full-body model.

During normal walking in the absence of foot slip, $\dot{x}_s = 0$ and the TMLIP model is identical to the conventional single-mass LIP model; during foot slip, $\dot{x}_s \neq 0$, and the TMLIP model explicitly captures the slip dynamics. We define the horizontal distance between the two masses as $\delta = x_c - x_s$ such that $\delta \geqslant 0$ when m_1 is anterior or in front of m_2 along the direction of walking. The TMLIP dynamic model is written as [13]

$$\ddot{\delta} = \omega_m^2(\delta + A), \tag{1}$$

where $A = 0$ and $\omega_m^2 = \omega^2$ are used for non-slip case and $A = \mu z_c$ and $\omega_m^2 = \frac{r_m}{r_m - 1}\omega^2$ with $r_m = \frac{m_1 + m_2}{m_1}$ for slip case. μ is the friction coefficient between the foot and the ground and $\omega = \sqrt{g/z_c}$ is the (constant) natural frequency, where g is gravitational constant.

B. Capture Point-Based Step Planning

The TMLIP model exhibits one unstable equilibrium, located at $\delta = -A$, $\dot{\delta} = 0$, and is referred to as the captured state of the model. The CP is defined as the stepping location which results in the model reaching the captured state [7]. From the solution to the TMLIP model [13], [14], the relative extension that is needed to reach a captured state is $\delta_0 = -A + \frac{\dot{\delta}}{\omega_m}$. Combining with the current COM location x_c, the CP for the TMLIP model is

$$\xi = x_c + \frac{\dot{\delta}}{\omega_m} - A. \tag{2}$$

Taking the time derivative of (2), we obtain

$$\dot{\xi} = \dot{x}_c + \frac{\ddot{\delta}}{\omega_m}. \tag{3}$$

Noting that $\dot{\delta} = \dot{x}_c - \dot{x}_s$, we substitute (1) and (2) into (3) and obtain the CP dynamics as

$$\dot{\xi} = \omega_m \left(\xi - x_s + \frac{\dot{x}_f}{\omega_m} + 2A \right). \tag{4}$$

Comparing (2) and (4) to the conventional CP $\xi = x + \frac{\dot{x}}{\omega}$ and its dynamics $\dot{\xi} = \omega(\xi - x_s)$, it is evident that the TMLIP is a generalization of the LIP model, that is, by setting the slipping velocity to zero and thus $A = 0$, $\omega_m = \omega$, $\dot{x}_s = 0$, and $\dot{\delta} = \dot{x}$.

Using the CP in (2), the stepping location is designed as

$$x_T = \hat{x}_c(T) + \lambda \frac{\dot{\delta}}{\omega_m} - A, \tag{5}$$

where $\hat{x}_c(T)$ is the predicted COM location at time T of the subsequent heel-strike, and λ is a parameter. For any forward progression $\dot{x}_c > 0$, $\lambda = 0$ leads to divergent motion with $\dot{x}_c \to \infty$, while $\lambda = 1$ leads to $\dot{x}_c \to 0$ by the definition of the CP above. For stable walking, $\lambda \in (0, 1)$ is selected. The velocity $\dot{x}_T$ is in turn calculated by taking the time derivative of (5) and by using (3), it can be written as

$$\dot{x}_T = \dot{\hat{x}}_c(T) + \lambda(\dot{\xi} - \dot{x}_c). \tag{6}$$

To ensure stability, the touchdown location velocity is selected to be constant, i.e., $\ddot{x}_T = 0$. The desired stepping location x_T in (5) and its derivatives in (6) is re-planned at every time step to ensure controller robustness.

III. Gait Recovery Control Design

A. Control System Overview

The previous section presents a stepping strategy under foot slip through an abstracted TMLIP model. To implement such stepping and other kinematic tasks, a whole-body robot controller is needed. The right schematic in Fig. 1 shows a 5-link planar model for the robotic walker. The geometry of both legs are symmetric. The generalized coordinate for the robot is denoted as $\boldsymbol{q} = [\theta_h^{st}\ \theta_k^{st}\ \theta_h^{sw}\ \theta_k^{sw}\ x_b\ z_b\ \theta_b]^T \in \mathbb{R}^7$, where x_b, z_b, and θ_b denote the horizontal and vertical position and rotation of the floating base, respectively. θ_h and θ_k are the thigh and the shank angles, and superscripts st and sw stand for stance and swing legs, respectively. Using the full-body dynamics that are built on $\boldsymbol{q}, \dot{\boldsymbol{q}}$ and $\ddot{\boldsymbol{q}}$, we will discuss the FWBOS-based control later in this section.

Fig. 2 illustrates the overall schematic of the gait recovery control design. The main variables (x_c, z_c, x_s) of the TMLIP model (i.e., COM and slipping foot motion) are computed and extracted from the 5-link full-body model. The TMLIP-model design provides the stepping location and its derivatives for gait recovery, which is implemented through the FWBOS-based design and joint torque compensation. The control system structure remains the same both for normal walking and slip recovery. Presence or absence of foot slip influences the step location given by the TMLIP and the use of switched WBOS- and FWBOS-based controllers.

B. WBOS and FWBOS Models

We first briefly review the WBOS-based controller and then present the FWBOS extension [18]. Using generalized coordinate $\boldsymbol{q}$, the robot dynamic model is specified by [15], [16]

$$\boldsymbol{D}\ddot{\boldsymbol{q}} + \boldsymbol{N}^T(\boldsymbol{b} + \boldsymbol{g}) + \boldsymbol{J}^T\boldsymbol{\Lambda}\dot{\boldsymbol{J}}\dot{\boldsymbol{q}} = (\boldsymbol{S}\boldsymbol{N})^T\boldsymbol{\tau}, \tag{7}$$

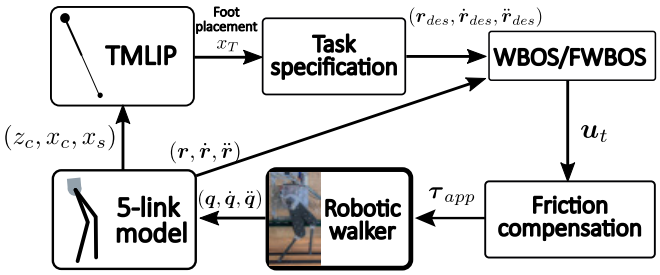

Fig. 2. Control diagram for walking. The schematics is identical for normal and slip walking. Slip changes the results of TMLIP and FWBOS calculations.

where $\boldsymbol{D} \in \mathbb{R}^{7\times7}$, $\boldsymbol{b}, \boldsymbol{g} \in \mathbb{R}^7$ are the inertia matrix, Coriolis and centrifugal forces, and gravity force vectors, respectively. $\boldsymbol{J} \in \mathbb{R}^{2\times7}$ and $\boldsymbol{\Lambda} \in \mathbb{R}^{7\times7}$ denote the support Jacobian and the mass inertia matrices, respectively, both associated with the contact point. $\boldsymbol{N} = \boldsymbol{I} - \boldsymbol{J}^+\boldsymbol{J} \in \mathbb{R}^{7\times7}$ is the dynamically consistent null-space of $\boldsymbol{J}$, where $\boldsymbol{J}^+ = \boldsymbol{D}^{-1}\boldsymbol{J}^T\boldsymbol{\Lambda}$ is the generalized inverse of $\boldsymbol{J}$. $\boldsymbol{S} \in \mathbb{R}^{4\times7}$ is the selection matrix which selects the rows of $\boldsymbol{q}$ that correspond to the actuated joints, and $\boldsymbol{\tau} \in \mathbb{R}^4$ are the joint torques. The joint torques are given by

$$\boldsymbol{\tau} = \boldsymbol{J}^{*T}\boldsymbol{F}_t, \tag{8}$$

where $\boldsymbol{J}^* = \boldsymbol{J}_t(\boldsymbol{S}\boldsymbol{N})^+$ is the support-consistent reduced Jacobian matrix, and $\boldsymbol{J}_t$ is the task Jacobian related to the generalized force $\boldsymbol{F}_t$. The task Jacobian enables the operator to move away from joint space and instead specifies the task in an arbitrary coordinate system, as shown later in this section. The task specification is done by the use of $\boldsymbol{F}_t$, which consists of acceleration $\boldsymbol{u}_t$ in task space, centrifugal and Coriolis forces $\boldsymbol{c}_t$, and gravity force $\boldsymbol{p}_t$, all expressed in task space, namely,

$$\boldsymbol{F}_t = \boldsymbol{\Lambda}_t\boldsymbol{u}_t + \boldsymbol{c}_t + \boldsymbol{p}_t. \tag{9}$$

Using the kinetic energy matrix $\boldsymbol{\Lambda}_t = (\boldsymbol{J}_t\boldsymbol{D}^{-1}\boldsymbol{J}_t^T)^{-1}$ and $\boldsymbol{J}_t^+ = \boldsymbol{D}^{-1}\boldsymbol{J}_t^T\boldsymbol{\Lambda}_t$, the above gravity and Coriolis/centrifugal contributions are expressed as $\boldsymbol{p}_t = \boldsymbol{J}_t^{+T}\boldsymbol{g}$ and $\boldsymbol{c}_t = \boldsymbol{J}_t^{+T}\boldsymbol{b} - (\boldsymbol{\Lambda}_t^T\dot{\boldsymbol{J}}_t - \boldsymbol{J}_t^{+T}\boldsymbol{J}^T\boldsymbol{\Lambda}\dot{\boldsymbol{J}})\dot{\boldsymbol{q}}$.

The above WBOS formulations are built upon the explicit assumption of no foot slip. We now extend these developments to relax the no-slip assumption and derive FWBOS. We write the general dynamic model where only the vertical component of the ground reaction force and movement is considered as

$$\boldsymbol{D}\ddot{\boldsymbol{q}} + \boldsymbol{b} + \boldsymbol{g} + \boldsymbol{J}_z^T F_z = \boldsymbol{S}^T\boldsymbol{\tau}, \tag{10}$$

where F_z is the vertical component of foot contact force and $\boldsymbol{J}_z = [0\ \ 1]\boldsymbol{J} \in \mathbb{R}^{1\times7}$ is a subset of $\boldsymbol{J}$ (i.e., the second row of the full contact Jacobian $\boldsymbol{J}$), which is used to describe the movement in vertical direction only. We multiply (10) by $\boldsymbol{J}_z\boldsymbol{D}^{-1}$ and obtain

$$\dot{v}_z - \dot{\boldsymbol{J}}_z\dot{q} + \boldsymbol{J}_z\boldsymbol{D}^{-1}(\boldsymbol{b} + \boldsymbol{g}) + \boldsymbol{J}_z\boldsymbol{D}^{-1}\boldsymbol{J}_z^T F_z = \boldsymbol{J}_z\boldsymbol{D}^{-1}\boldsymbol{S}^T\boldsymbol{\tau},$$

where the contact point vertical velocity is $v_z = \boldsymbol{J}_z\dot{\boldsymbol{q}}$ and its derivative $\dot{v}_z = \boldsymbol{J}_z\ddot{\boldsymbol{q}} + \dot{\boldsymbol{J}}_z\dot{\boldsymbol{q}}$ are used. By using $\boldsymbol{J}_z$, v_z represents only the vertical velocity of the contact point. Since the stance foot remains on the ground, therefore $v_z = \dot{v}_z = 0$ and from the above equation, the contact force is obtained as

$$F_z = \boldsymbol{\Lambda}_z\dot{\boldsymbol{J}}_z\dot{q} - \left(\boldsymbol{J}_z^+\right)^T(\boldsymbol{b} + \boldsymbol{g}) + \left(\boldsymbol{J}_z^+\right)^T\boldsymbol{S}^T\boldsymbol{\tau}, \tag{11}$$

where $\boldsymbol{J}_z^+ = \boldsymbol{D}^{-1}\boldsymbol{J}_z^T\boldsymbol{\Lambda}_z$ and $\boldsymbol{\Lambda}_z = (\boldsymbol{J}_z\boldsymbol{D}^{-1}\boldsymbol{J}_z^T)^{-1}$. Since the reduced Jacobian $\boldsymbol{J}_z$ constrains the vertical direction only, F_z is a scalar representing the normal (z-axis) component of the ground reaction force.

Considering a Coulomb friction model, the frictional contact force is denoted as $\boldsymbol{F}_{tot} = \begin{bmatrix}\mp\mu F_z & F_z\end{bmatrix}^T$, where $F_x = \mp\mu F_z$ and "$-\mu$" is used if the slip is in the positive x direction and vice versa. Defining friction matrix $\boldsymbol{\mu} = \begin{bmatrix}\mp\mu & 1\end{bmatrix}^T$, the contact force is expressed as $\boldsymbol{F}_{tot} = \boldsymbol{\mu}F_z$. The frictional contact force $\boldsymbol{F}_{tot}$ is then plugged back into (10), where the reduced contact Jacobian is replaced with the full form

$$\boldsymbol{D}\ddot{\boldsymbol{q}}+\boldsymbol{b}+\boldsymbol{g}+\boldsymbol{J}^T\boldsymbol{F}_{tot} = \boldsymbol{D}\ddot{\boldsymbol{q}}+\boldsymbol{b}+\boldsymbol{g}+\boldsymbol{J}^T\boldsymbol{\mu}F_z = \boldsymbol{S}^T\boldsymbol{\tau}. \quad (12)$$

Combining (11) and (12), projecting to task space and defining $\boldsymbol{N}_f^T = \boldsymbol{I} - \boldsymbol{J}^T\boldsymbol{\mu}\left(\boldsymbol{J}_z^+\right)^T$, we obtain the joint torque

$$\boldsymbol{\tau} = \boldsymbol{J}_f^{*T}\boldsymbol{F}_t^F, \quad (13)$$

where $\boldsymbol{J}_f^* = \boldsymbol{J}_t(\boldsymbol{S}\boldsymbol{N}_f)^+$ and $(\boldsymbol{S}\boldsymbol{N}_f)^+ = \boldsymbol{D}^{-1}(\boldsymbol{S}\boldsymbol{N}_f)^T\left(\boldsymbol{S}\boldsymbol{N}_f\boldsymbol{D}^{-1}(\boldsymbol{S}\boldsymbol{N}_f)^T\right)^{-1}$. The generalized force is given by

$$\boldsymbol{F}_t^F = \boldsymbol{\Lambda}_t^T\boldsymbol{u}_t + \boldsymbol{c}_t^F + \boldsymbol{p}_t^F, \quad (14)$$

where $\boldsymbol{p}_t^F = (\boldsymbol{J}_t^+)^T\boldsymbol{N}_f^T\boldsymbol{g}$ is the gravitational contribution and $\boldsymbol{c}_t^F = (\boldsymbol{J}_t^+)^T\boldsymbol{N}_f^T\boldsymbol{b} - (\boldsymbol{\Lambda}_t^T\dot{\boldsymbol{J}}_t - (\boldsymbol{J}_t^+)^T\boldsymbol{\mu}\boldsymbol{\Lambda}\dot{\boldsymbol{J}}_z)\dot{\boldsymbol{q}}$ denotes the Coriollis/centrifugal forces.

C. Task Specification

We need to define the task space of the WBOS and FWBOS controller. For bipedal walking gaits, the task vector specifies the COM height z_c, the angle of the torso θ_b, the horizontal and vertical swing foot positions x_{sw} and z_{sw}, respectively; see Fig. 1. The task vector is therefore defined as $\boldsymbol{r} = \begin{bmatrix}z_c & \theta_b & x_{sw} & z_{sw}\end{bmatrix}^T$. We need to specify the walking gait by the desired task vector $\boldsymbol{r}_{des}$ such that under the joint torque control, $\boldsymbol{r}$ converges to $\boldsymbol{r}_{des}$.

The desired task vector is designed and specified as follows. The desired COM height z_c^d and the desired torso orientation angle θ_b^d are chosen as constant. The desired horizontal location of the swing foot x_{sw}^d is designed to smoothly track between the takeoff and touchdown location such that x_{sw} arrives at x_T at $t = T$ that is given by (5). We use a 5th-order polynomial function to determine x_{sw}^d, that is, $x_{sw}^d(t) = \sum_{i=0}^5 a_i t^i$, where coefficients a_i, $i = 0, \ldots, 5$, are selected using the current position $x_{sw}(t)$ and velocity $\dot{x}_{sw}(t)$ at current time t and the desired position $x_{sw}(T) = x_T$ by (5) and velocity $\dot{x}_{sw}(T) = \dot{x}_T$ by (6), and acceleration $\ddot{x}_{sw}^d(T) = 0$, which are specified by the step planner presented in the previous section. The desired trajectory is recalculated at every time instance to take into account disturbances and uncertainties.

The desired vertical location z_{sw}^d of the swing foot is mainly specified by a sine wave. To ensure that the free foot touches the ground, a decreasing quadratic term is added to the desired z_{sw} profile, and therefore, the complete desired trajectory for z_{sw} is designed as

$$z_{sw}^d(t) = \frac{z_0}{2}\left[1 - \cos(\omega_f t)\right] - z_1(\omega_f t)^2, \quad (15)$$

where $\omega_f > 0$ is a constant frequency, constant z_0 is the maximum desired height of the foot and z_1 is a constant parameter that ensures that the swing foot contacts the ground at $t = T$, i.e., $z_{sw}^d(T) = 0$. The desired task vector is then $\boldsymbol{r}_{des} = \begin{bmatrix}z_c^d & \theta_b^d & x_{sw}^d(t) & z_{sw}^d(t)\end{bmatrix}^T$ and the desired velocity $\dot{\boldsymbol{r}}_{des}$ and acceleration $\ddot{\boldsymbol{r}}_{des}$ are obtained by taking the time derivative of $\boldsymbol{r}_{des}$ using (15) and above discussions.

D. Controller Design

We need to design the task acceleration $\boldsymbol{u}_t$ that is used in (9) and (14) as the control input. A proportional and derivative controller is designed to generate the desired task acceleration as

$$\boldsymbol{u}_t = \ddot{\boldsymbol{r}}_{des} - \boldsymbol{k_p}\boldsymbol{e} - \boldsymbol{k_d}\dot{\boldsymbol{e}}, \quad (16)$$

where tracking error $\boldsymbol{e} = \boldsymbol{r} - \boldsymbol{r}_{des}$, and $\boldsymbol{k_p}, \boldsymbol{k_d} \in \mathbb{R}^{4\times4}$ are the diagonal gain matrices (with positive diagonal elements). Under (16) and using the control input $\ddot{\boldsymbol{r}} = \boldsymbol{u}_t$, we obtain the error dynamics

$$\ddot{\boldsymbol{e}} + \boldsymbol{k}_p\boldsymbol{e} + \boldsymbol{k}_d\dot{\boldsymbol{e}} = \boldsymbol{0}.$$

Therefore, the asymptotic stability is obtained since $\boldsymbol{k}_p$ and $\boldsymbol{k}_d$ are selected as diagonal matrices with positive elements. Asymptotic stability in the task space holds in joint space if the transformations are fully determined, i.e., if the Jacobians are full-rank.

The above robot control (16) does not consider and compensate for friction effects in the robot dynamics. In experimental implementation, we included a friction compensation mechanism to counteract the effects of friction. The actual implemented joint torque is $\boldsymbol{\tau}_{app} = \boldsymbol{\tau} + \boldsymbol{\tau}_f$, where $\boldsymbol{\tau}_{app}$ is the actually applied joint torque and $\boldsymbol{\tau}$ is the torque calculated by the full-body controller given in (8) or (13). The compensation drive torque $\tau_{f,i}$, ith element of $\boldsymbol{\tau}_f$ for robot joints, $i = 1, 2, 3, 4$, is designed as

$$\tau_{f,i} = \begin{cases} f_i\,\mathrm{sign}(\dot{q}_i), & |\dot{q}_i| \geqslant \dot{q}_{st}, \\ f_i\,\mathrm{sign}(\tau_i), & |\dot{q}_i| < \dot{q}_{st}, \end{cases} \quad (17)$$

where f_i is the frictional torque for the ith robot drive joint and is identified and obtained experimentally. $\dot{q}_i$ is the velocity of the ith joint and $\dot{q}_{st}$ is the threshold for the joint velocity.

IV. Experiments

Fig. 3(a) shows the hardware platform of a 7-DOF planar bipedal robot and Fig. 3(b) for the experimental setup. We designed and fabricated the bipedal robot primarily for the slip recovery gait control. The floating-base torso is mounted via a high-precision, low-friction rotational bearing to a sub-carriage, giving the torso to freely rotate around the pitch axis. The carriage is equipped with two high-precision, low-friction linear sliders, allowing the sub-carriage to freely move vertically. The carriage set is affixed to a rigid rail by two low-friction rollers, which allows it to freely move horizontally. With the rail, sliders, and bearing, the floating-base torso is confined to the sagittal plane and can move freely in the horizontal and vertical directions, as well as freely rotate around the pitch axis. At the same time, the carriage system

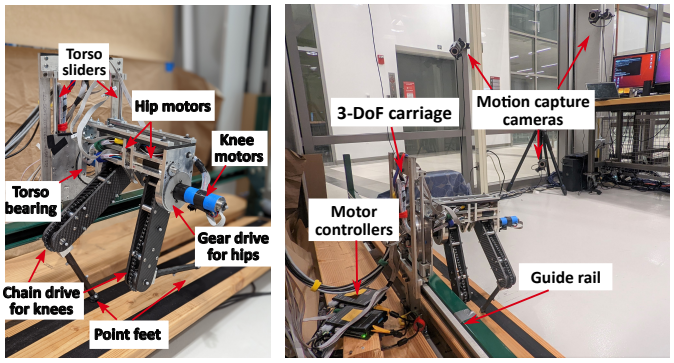

(a) (b)

Fig. 3. (a) The 7-DOF bipedal robotic walker prototype. (b) The indoor experimental setup with the robot control systems and high- and low-friction ground conditions.

prevents any movement of the robot in the lateral direction and around the roll and the yaw axes.

Two parallel-chain legs are attached to the torso and each leg consists of two rigid links. The robotic feet are ball-shaped and made of acetal polymer. Due to the small radius (around 9.5 mm), the rolling effects of the robot feet are not significant and can be treated as point feet. The two hip and two knee joints are actuated by 4 brushless motors (model DC-MAX26S from Maxon Inc., Switzerland). The hip-joint motors are positioned inside the torso, while the knee-join motors are located outside the body. All motors are integrated with high-ratio gearboxes and knee joints are driven by two chains. Each motor is equipped with a rotational encoder with a resolution of 1024 pulses per turn. In addition, a motion capture system (9 Vantage cameras from Vicon Ltd., Oxford, UK) was used to measure the positions and velocities of the linear joints which did not have corresponding encoders; see Fig. 3(b). The foot slip detection was also obtained in real time by using the captured motion data. The Robot Operating System (ROS) was used to collect the data from the encoders and the motion capture system, and command the real-time robot control. The control algorithm was running at 115 Hz. The proposed WBOS and FWBOS control algorithm was first developed and verified in Matlab simulation environment. The simulation-verified control algorithms were translated to C++ to deploy the real-time implementation on the robotic walker platform.

In order to selectively induce slip, various tapes were applied to the floor to create ground surfaces with three levels of friction coefficients. The robotic foot was made of hard plastic material. When we used anti-slip tapes on the floor, the friction coefficient of the foot-floor contact was high around $\mu = 0.5$. When we coated the floor with painter's tape, the friction coefficient of the foot-floor contact was low around $\mu = 0.2$. Besides these two types of ground surfaces, we also taped a hard plastic sheet on the floor and this would bring extremely low friction coefficient around $\mu \approx 0.1$. The friction coefficient of each foot-floor surface was estimated experimentally by using a force plate to measure the friction force. The robot's feet were manually pushed and dragged to slide on the taped surfaces mounted on the multi-axis force plate. The friction coefficient was calculated as a ratio between the tangential and normal forces from these experiments.

The accuracy of the robot dynamic model is critical to the performance of the proposed controller. Table I lists a partial set of the model parameters values that can be precisely measured. The remaining model parameters such as moments of angular inertia for thigh I_h, shank with the motor I_k, shank without the motor $I_{k,r}$, and COM locations for thigh L_{ch} and shank L_{ck} cannot be measured directly. We therefore performed system identification to identify the parameters and verify that the model structure matches the experimental setup. System identification was performed on the subsystem for each leg individually. Table II lists the values for the sets of lumped parameters for both legs. The experimental estimates for all the inertial model parameters show good agreement between the two legs and the design model values. The two non-inertial lumped parameters (i.e., $m_h L_{ch} + m_k L_h$ and $m_k L_{ck}$) exhibit more variability. The discrepancies are due to the used gait excitation predominately excited the inertial forces while the Coriolis/centrifugal contribution remained almost negligible.

TABLE I
MODEL PARAMETERS OF THE EXPERIMENTAL BIPEDAL ROBOT.

Parameter	Symbol	Value
Torso length	L_b	2.5 cm
Thigh length	L_h	20 cm
Shank length	L_k	22 cm
Mass of the torso	m_b	3.600 kg
Mass of the thigh	m_h	1.074 kg
Mass of the shank	m_k	0.190 kg

TABLE II
IDENTIFICATION OF LUMPED PARAMETERS FOR EACH LEG

Lumped Parameters	Unit	Model estimate	Left/Right leg (Exp.)
$I_h + m_h L_{ch}^2 + m_k L_h^2$	[kg m^2]	0.057	0.062/0.052
$I_k + m_k L_{ck}^2$	[kg m^2]	0.037	0.038/0.039
$I_{k,r} + m_k L_{ck}^2$	[kg m^2]	0.001	0.000/0.001
$m_h L_{ch} + m_k L_h$	[kg m]	0.074	$0.085/-0.002$
$m_k L_{ck} L_h$	[kg m^2]	0.001	0.002/0.001
$m_k L_{ck}$	[kg m]	0.005	0.014/0.003

We also conducted experiments to identify and estimate robot joint drive frictions. The drive friction torques in (17) were estimated as: $f_1 = 0.15$, $f_2 = 0.06$, $f_3 = 0.18$, and $f_4 = 0.06$ Nm. $\dot{q}_{st} = 0.1$ rad/s was selected as the threshold in friction compensation calculation in (17). For desired task vector profile $\boldsymbol{r}_{des}$, we chose $z_c^d = 33$ cm, $\theta_b^d = 0$, $z_0 = 4$ cm, $z_1 = 2$ cm, and $\omega_f = 2.5$ s^{-1} for (15). For controller (16), we chose $\boldsymbol{k}_p = \text{diag}(80, 100, 300, 12)$ and $\boldsymbol{k}_d = \text{diag}(1, 2, 35, 5)$ in experiments.

V. EXPERIMENTAL RESULTS

We first present the normal walking results without foot slip. Fig. 4(a) shows the trajectory tracking results for normal (non-slip) walking under the WBOS controller. The figure includes the tracking error profiles, that is, tracking errors for the COM vertical position z_c, torso orientation θ_b, and horizontal and vertical positions x_{sw} and z_{sw} for the swing

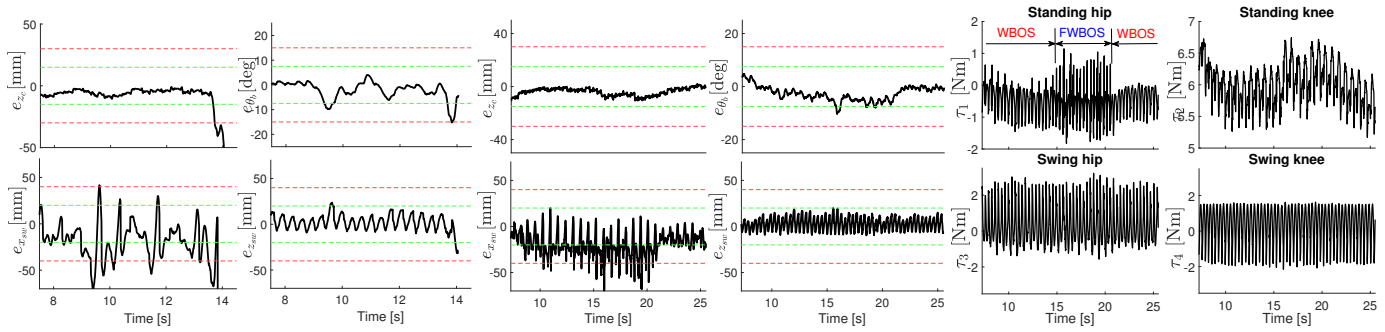

(a) (b) (c)

Fig. 5. Components of the task vector errors $\boldsymbol{e} = \boldsymbol{r} - \boldsymbol{r}_{des} = [e_{x_c}\ e_{\theta_b}\ e_{x_{sw}}\ e_{z_{sw}}]$ on ground with friction coefficients switching between high-friction ($\mu = 0.5$) and low-friction surface ($\mu = 0.2$) under (a) the WBOS controller and (b) the FWBOS controller. (c) Joint torques for successful slip recovery using a switched WBOS/FWBOS controller.

foot. It is clear that both the COM vertical position and torso orientation follow the constant values closely under the controller. The error of the swing foot's vertical position is periodic, which is a consequence of a small lag between the desired and actual trajectories. The error of the swing foot's horizontal position is among the largest and most variable. Fig. 4(b) further shows the horizontal location of the swing foot along with the designed touchdown location. For each time step, the desired horizontal position x_{sw}^d meets the desired touchdown location x_T. From Fig. 4, the swing foot horizontal often lagged up to 2 cm behind the desired profile. However, the system dynamics are mainly determined by the position of the swing foot at the end of each step, which converges to the desired positions.

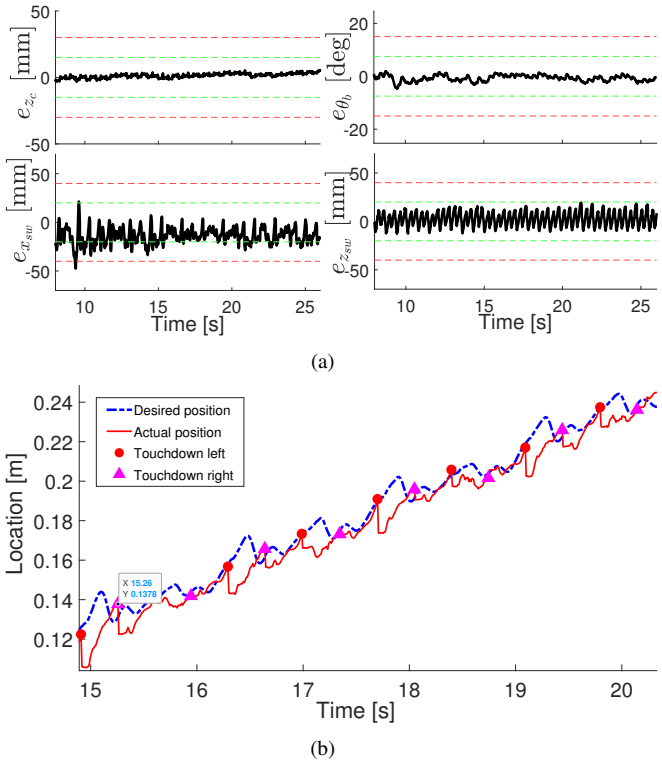

(a)

(b)

Fig. 4. Normal walking performance under the WBOS control on high-friction ground surface ($\mu = 0.5$). (a) Components of the task vector errors $\boldsymbol{e} = \boldsymbol{r} - \boldsymbol{r}_{des} = [e_{x_c}\ e_{\theta_b}\ e_{x_{sw}}\ e_{z_{sw}}]$. (b) Swing foot positioning. At the end of the step, the actual location converged towards desired location.

To examine the controller's performance under foot slip, the robot was set in motion continuously on ground surfaces with a mixed friction coefficients between high-friction ($\mu = 0.5$) and high-friction coefficients ($\mu = 0.2$). Fig. 5(a) shows the task tracking errors for the slip-and-fall case when the WBOS-based controller was used. For the first part of the trial until $t = 13.0$ s, the robot performed normal walking without foot slip under the WBOS controll on high-friction surface ($\mu = 0.5$), similar to that in Fig. 4(a). Upon touching down on the low-friction surface ($\mu = 0.2$) at $t = 13.0$ s, the robot's stance foot started to slip backwards and the robot lost balance. Despite touching down with the other foot, the robot cannot regain balance resulting in a fall under the WBOS controller. After the onset of foot slip, all four components of the task error $\boldsymbol{e}$ deviated significantly from the desired quantities.

We repeated the same experiment but switched to the FWBOS controller when the foot hit on a low-friction surface. The robot was able to maintain balance through the transitions from the high- to the low-friction ground as well as maintain a periodic forward progression despite occurrence of foot slip. Fig. 5(b) shows the tracking errors for the successful slip recovery when the FWBOS controller was used. Same to the above-discussed WBOS control, at $t = 14.5$ s, the robot reached the low-friction portion of the walkway. The foot slipped at each step but yet the robot was able to maintain balance. The results show that foot slip led to larger deviations for task tracking and the FWBOS controller contained the deviations and kept the tracking error within acceptable bounds.

Fig. 5(c) further shows the joint torques $\boldsymbol{\tau}$ with the switch from the WBOS to the FWBOS controllers when the robot entered the low-friction ground surface. The swing leg actuation exhibited a periodic profile throughout the walk, regardless of the presence or absence of foot slip. This was expected as the swing leg dynamics was dominated by inertial forces that mostly remain unchanged due to periodic lifting and lowering of the foot. The mean value for the actuation of the swing leg hip was positive and this was expected given the knee is bent and thus was always in front of the torso. The offset of the swing hip torque provided a compensating force for the gravitational forces of the swing leg. The actuation of the standing leg showed significant change due to the presence of foot slip starting at time $t = 14.5$ s (and ending at

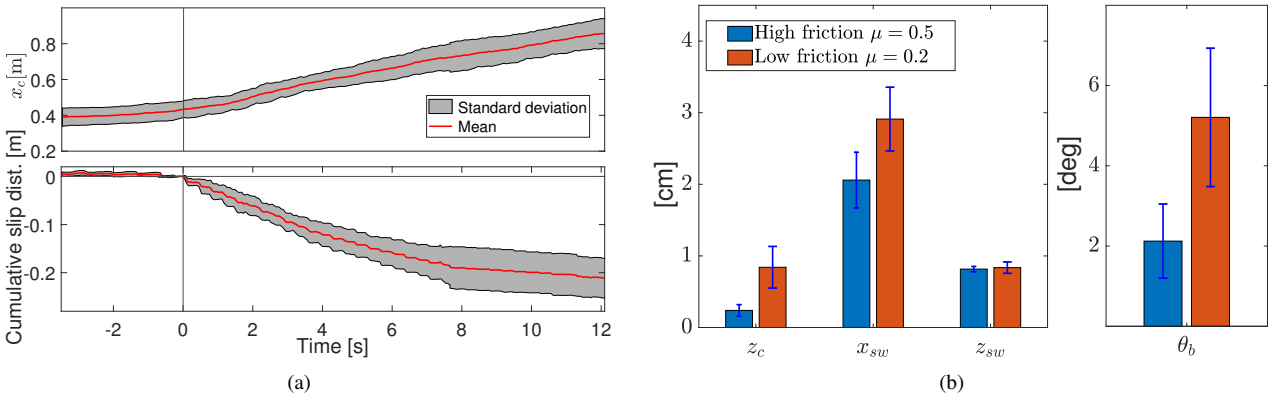

(a) (b)

Fig. 7. (a) Top: Mean and standard deviation of the horizontal COM position x_c of the robot. Bottom: Mean and standard deviation of cumulative slipping distance of the stance leg on low-friction surface ($\mu = 0.2$) under the FWBOS controller. (b) The means and standard deviations errors of the trajectories of robot COM vertical position z_c, horizontal and vertical positions (x_{sw} and z_{sw}) of the swing foot, and the rotation (θ_b) of the floating torso base on the high ($\mu = 0.5$) and low ($\mu = 0.2$) friction surfaces under the FWBOS controller.

around $t = 20.5$ s). In response, the FWBOS controller was initiated at this moment. It is clear from Fig. 5(c) that the FWBOS controller generated a large, positive torque on the hip joint. This increased torque resulted in a forward force on the contact foot and caused the slip to stop. It was also evident that while both the WBOS and FWBOS controllers prescribed continuous actuation in the absence of heel-strike, the switch between the two controllers represents a discrete jump in actuation. Finally, the torque on the stance knee was higher during walking on the slippery surface than on the high-friction surface. As seen in Fig. 5(b), the COM lowered due to slippage at each step, resulting in further bending of the stance knee and an increase of actuation torque.

Fig. 6 shows the comparison of the COM's forward velocity as function of stride progression variable under the WBOS and FWBOS controllers on high (non-slip) and low (slip) friction surfaces. The stride progression variable is normalized by the steady-state step period under non-slip steady gait. The robot converged to periodic stepping gait both in absence (non-slip) and presence of foot slip under the FWBOS controller. However, the robot cyclic gait became unstable with foot slip under the WBOS controller. The COM velocity variation was greater for the slip case, which is expected as the slip moves the foot contact point and changes the progression curves.

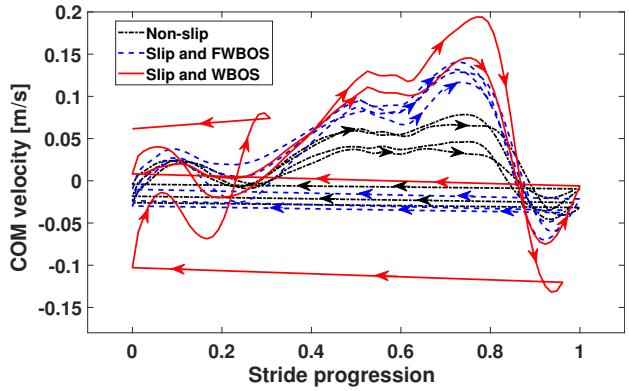

Fig. 6. Performance comparison as the diagrams shown by the COM's velocity vs. walking stride progression under non-slip and foot slip under the WBOS and FWBOS controllers. The arrows indicate the motion progression direction with time.

We conducted additional experiments and obtained multiple runs on the same ground as well as on surfaces with different friction coefficients. Fig. 7 shows the FWBOS control performance under repeated experimental trials. Fig. 7(a) shows the mean and standard deviation of the trajectories of the horizontal robot COM position x_c and cumulative slipping distance of the stance leg over 5 trials on low-friction surface ($\mu = 0.2$) under the FWBOS controller. It is clear that under the FWBOS controller, the bipedal robot consistently performed a stable gait on low-friction surfaces. Fig. 7(b) further shows the statistical results of the 5 experimental trials separately on both the high ($\mu = 0.5$) and low ($\mu = 0.2$) friction surfaces. The plot includes the mean and standard deviations of the error trajectories for the robot COM vertical position z_c, horizontal and vertical positions (x_{sw} and z_{sw}) of the swing foot, and the rotation (θ_b) of the floating torso base. These results clearly demonstrate the robust performance of the controller from multiple runs.

We conducted additional experiments for the robot to walk on the extremely low-friction ground surface with $\mu \approx 0.1$. In this case, the extremely low friction foot-ground contact resulted in a slip-induced fall under either of the WBOS or FWBOS controllers. Fig. 8(a) shows the swing foot location and step progression under both the WBOS and FWBOS controllers. At $t = 0$ s, the robot foot touched down on the extremely low-friction surface. A recovery attempt is clearly visible due to higher discrepancies between the desired and actual positions. Compared to the WBOS controller for stable gait lasting for about 1 s, the FWBOS controller maintained longer time balance for about 2.5 s on the slippery surface before falling down. Fig. 8(b) shows the slipping distance for the stance foot in the experiment. The WBOS controller was able to maintain stability for two steps and resulted in a fall on the third step after the onset of slip. In contrast, the FWBOS controller was able to maintain stability for 6 steps and finally the robot fell at the 7th step of the recovery sequence. The results also demonstrate the slipping distance which leads to robot's fall. Under the WBOS control, the slipping distance was about 30 mm before the robot fell in the subsequent step. In the FWBOS control trial, the gait also experienced a 30 mm foot slip; however, that did not immediately lead to fall. The

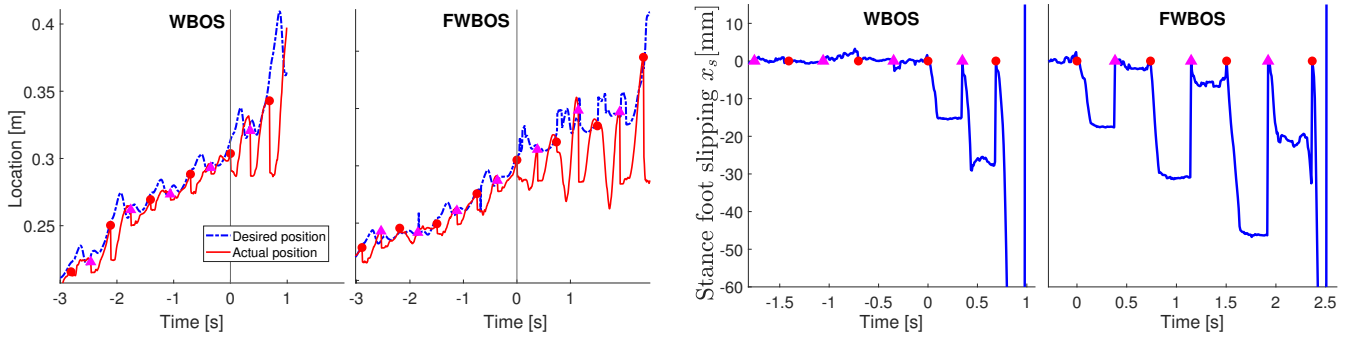

(a) (b)

Fig. 8. Comparison performance of the WBOS and FWBOS controllers for robot walking on extremely low-friction coefficient surfaces ($\mu \approx 0.1$). (a) Swing foot positions and (b) stance foot slipping distances during each step. Time $t = 0$ denotes the onset of foot slip. The magenta triangle markers "▲" and red circular markers "●" represent the right- and left-leg touchdown positions, respectively.

controller was able to stabilize the walking gait under slip with a distance upwards to 50 mm before resulting in a fall.

The FWBOS balance controller can handle limited model uncertainties as the precise model for the custom built was needed. Due to page limit, we did not conduct simulation study to explore the robustness of the FWBOS control. The targeted balance recovery motion profile was planned by the high-level TMLIP model-based method that explicitly incorporated the slip dynamics. Therefore, the integrated TMLIP-FWBOS design can handle certain model uncertainties.

VI. Conclusion

The presented work in this paper introduced a bipedal walking controller with key feature to maintain the balance walking gaits under foot slip. This was achieved by using the integrated TMLIP model with the FWBOS control design. The TMLIP model provided a stepping location design and the FWBOS controller was used to obtain joint torques to compensate for slip dynamics. We presented the 5-link planar bipedal walking robot as an experimental platform. The effectiveness of the controller was demonstrated by a series of experiments examining robotic walking over slippery ground surface. The experimental results consistently confirmed that the FWBOS controller outperformed the benchmark control on low-frictional surfaces in term of gait stability recovery. We also presented a scenario with extremely low-friction ground condition in which none of the presented controllers was able to maintain gait balance. Compared to a conventional controller, the FWBOS controller still outperformed in term of maintaining balance time and walking distance .

References

[1] C. G. Atkeson *et al.*, "No falls, no resets: Reliable humanoid behavior in the darpa robotics challenge," in *Proc. IEEE Int. Conf. Humanoid Robots*, Seoul, Korea, 2015, pp. 623–630.

[2] M. Khadiv, S. A. A. Moosavian, A. Yousefi-Koma, M. Sadedel, and S. Mansouri, "Optimal gait planning for humanoids with 3d structure walking on slippery surfaces," *Robotica*, vol. 35, no. 3, pp. 569–587, 2017.

[3] J. Reher and A. D. Ames, "Dynamic walking: Toward agile and efficient bipedal robots," *Ann. Rev. Contr. Robot. Auton. Syst.*, vol. 4, pp. 535–572, 2021.

[4] S. Kajita, F. Kanehiro, K. Kaneko, K. Yokoi, and H. Hirukawa, "The 3d linear inverted pendulum mode: A simple modeling for a biped walking pattern generation," in *Proc. IEEE/RSJ Int. Conf. Intell. Robot. Syst.*, Osaka, Japan, 2001, pp. 239–246.

[5] S. Caron, A. Escande, L. Lanari, and B. Mallein, "Capturability-based pattern generation for walking with variable height," *IEEE Trans. Robotics*, vol. 36, no. 2, pp. 517–536, 2020.

[6] X. Xiong and A. Ames, "3-d underactuated bipedal walking via h-lip based gait synthesis and stepping stabilization," *IEEE Trans. Robotics*, vol. 38, no. 4, pp. 2405–2425, 2022.

[7] J. Pratt, J. Carff, S. Drakunov, and A. Goswami, "Capture point: A step toward humanoid push recovery," in *Proc. IEEE Int. Conf. Humanoid Robots*, Genova, Italy, 2006, pp. 200–207.

[8] T. Koolen, T. de Boer, J. Rebula, A. Goswami, and J. Pratt, "Capturability-based analysis and control of legged locomotion, Part 1: Theory and application to three simple gait models," *Int. J. Robot. Res.*, vol. 31, no. 9, pp. 1094–1113, 2012.

[9] J. Englsberger, C. Ott, and A. Albu-Schäeffer, "Three-dimensional bipedal walking control based on divergent component of motion," *IEEE Trans. Robotics*, vol. 31, no. 2, pp. 355–368, 2015.

[10] M. Khadiv, A. Herzog, S. A. A. Moosavian, and L. Righetti, "Walking control based on step timing adaptation," *IEEE Trans. Robotics*, vol. 36, no. 3, pp. 629–643, 2020.

[11] Y. Gong and J. W. Grizzle, "Zero dynamics, pendulum models, and angular momentum in feedback control of bipedal locomotion," *ASME J. Dyn. Syst., Meas., Control*, vol. 144, no. 6, 2022, article 121006.

[12] K. Chen, M. Trkov, J. Yi, Y. Zhang, T. Liu, and D. Song, "A robotic bipedal model for human walking with slips," in *Proc. IEEE Int. Conf. Robot. Autom.*, Seattle, WA, 2015, pp. 6301–6306.

[13] M. Mihalec, M. Trkov, and J. Yi, "Recoverability-based optimal control for a bipedal walking model with foot slip," in *Proc. Amer. Control Conf.*, New Orleans, LA, 2021, pp. 1766–1771.

[14] ——, "Balance recoverability and control of bipedal walkers with foot slip," *ASME J. Biomech. Eng.*, vol. 144, no. 5, 01 2022.

[15] L. Sentis, "Synthesis and control of whole-body behaviors in humanoid systems," Ph.D. dissertation, Stanford Univ., Stanford, CA, 2007.

[16] D. Kim, Y. Zhao, G. Thomas, B. R. Fernandez, and L. Sentis, "Stabilizing series-elastic point-foot bipeds using whole-body operational space control," *IEEE Trans. Robotics*, vol. 32, no. 6, pp. 1362–1379, 2016.

[17] J. Luo, Y. Su, L. Ruan, Y. Zhao, D. Kim, L. Sentis, and C. Fu, "Robust bipedal locomotion based on a hierarchical control structure." *Robotica*, vol. 37, no. 10, pp. 1750–1767, 2019.

[18] M. Mihalec and J. Yi, "Control of a bipedal walker under foot slipping condition using whole-body operational space framework," *IFAC PapersOnLine*, vol. 54-20, pp. 278–283, 2021.

[19] M. Trkov, K. Chen, and J. Yi, "Bipedal model and hybrid zero dynamics of human walking with foot slip," *ASME J. Comput. Nonlinear Dyn.*, vol. 14, no. 10, 2019, 101002.

[20] T. Chen and B. Goodwine, "Robust gait design for a compass gait biped on slippery surfaces," *Robot. Auton. Syst.*, vol. 140, 2021, article 103762.

[21] M. Mihalec, F. Han, and J. Yi, "Integrated inverted pendulum and whole-body control design for bipedal robot with foot slip," *IFAC PapersOnLine*, vol. 55-37, pp. 376–381, 2022.

[22] J. P. Ferreira, G. Franco, P. A. Coimbra, and M. Crisóstomo, "Human-like gait adaptation to slippery surfaces for the NAO robot wearing instrumented shoes," *Intl. J. Humanoid Robot.*, vol. 17, no. 3, 2020, article 2050007.

[23] W.-L. Ma, Y. Or, and A. D. Ames, "Dynamic walking on slippery surfaces: Demonstrating stable bipedal gaits with planned ground slippage," in *Proc. IEEE Int. Conf. Robot. Autom.*, Montreal, Canada, 2019, pp. 3705–3711.